

Nanoscale

Accepted Manuscript



This is an *Accepted Manuscript*, which has been through the Royal Society of Chemistry peer review process and has been accepted for publication.

Accepted Manuscripts are published online shortly after acceptance, before technical editing, formatting and proof reading. Using this free service, authors can make their results available to the community, in citable form, before we publish the edited article. We will replace this *Accepted Manuscript* with the edited and formatted *Advance Article* as soon as it is available.

You can find more information about *Accepted Manuscripts* in the [Information for Authors](#).

Please note that technical editing may introduce minor changes to the text and/or graphics, which may alter content. The journal's standard [Terms & Conditions](#) and the [Ethical guidelines](#) still apply. In no event shall the Royal Society of Chemistry be held responsible for any errors or omissions in this *Accepted Manuscript* or any consequences arising from the use of any information it contains.

PAPER

Surface-Dominated Transport and Enhanced Thermoelectric Figure of Merit in Topological Insulator $\text{Bi}_{1.5}\text{Sb}_{0.5}\text{Te}_{1.7}\text{Se}_{1.3}$

Cite this: DOI: 10.1039/x0xx00000x

Received 00th September 2014,

Accepted 00th September 2014

DOI: 10.1039/x0xx00000x

www.rsc.org/nanoscale

Te-Chih Hsiung,^{a,b,c*} Chung-Yu Mou,^d Ting-Kuo Lee,^{a,c} and Yang-Yuan Chen^{c,e*}

We report an observation of an order of magnitude enhancement of the thermoelectric figure of merit ($ZT=0.36$) in topological insulator $\text{Bi}_{1.5}\text{Sb}_{0.5}\text{Te}_{1.7}\text{Se}_{1.3}$ nanowires at 300 K as compared with its bulk specimen ($ZT=0.028$). The enhancement was primarily due to an order of magnitude increase of electrical conductivity of the surface-dominated transport and thermally activated charge carriers in the nanowires. Magnetoresistance analysis revealed the presence of Dirac electrons and determined the Fermi level near the conduction band edge. This might be the first thermoelectric measurement of samples with a chemical potential in the gap of topological insulator without gate tuning and provides an opportunity to study the contribution of surface states to Seebeck coefficient and resistivity without concern for the complex effect of band bending.

1 Introduction

The unique electronic structure of gapless surface states and bulk gap^{1–5} in topological insulators (TIs) create a unique opportunity for applying them in thermoelectric (TE) applications.⁶ The efficiency of TE material is characterized by the dimensionless figure of merit (ZT) ($= S^2T/\rho\kappa$), where T , S , ρ , and κ are the absolute temperature, Seebeck coefficient, electrical resistivity, and thermal conductivity, respectively. Power factor (PF, $S^2\sigma$) enhancement can be obtained by creating a resonant state near the Fermi level because of the drastic change in the electronic density of state.⁷ Phonon boundary scattering substantially reduces thermal conductivity in nanowires (NWs),^{8,9} and confinement effects are predicted to enhance the PF.¹⁰ After the novel surface state in TIs was discovered, the effect of the nontrivial topology on the TE properties became an appealing scientific topic.^{6,11–13} Because NWs exhibit more surface states than bulk materials and nanoflakes do, we were able to observe the novel TE properties of TI NWs. The enhancement of TE ZT in TIs has been theoretically proposed⁶; however, experimental results have revealed that the TE PF in low-dimensional TIs is still lower than that of their parent bulk materials.^{11–13}

Although the TE properties of $\text{Bi}_{1.5}\text{Sb}_{0.5}\text{Te}_{1.7}\text{Se}_{1.3}$ (BSTS) bulk materials and nanoflakes have been investigated, the NWs of the system have yet to be explored. In this paper, we report an observation of an order of magnitude enhancement of ZT ($=0.36$) in TI $\text{Bi}_{1.5}\text{Sb}_{0.5}\text{Te}_{1.7}\text{Se}_{1.3}$ NWs at 300 K. The enhancement was primarily due to an order of magnitude increase of the electrical conductivity (2.38×10^5 S/m) of the surface-dominated transport and thermally activated charge carriers in NWs, compared with their counterpart BSTS bulk materials. This might be the first TE measurement of samples with a chemical potential in the gap of TI without gate tuning, and provides an opportunity to study the

contribution of surface states to Seebeck coefficient and resistivity without concern for the complex effect of band bending.

The recently discovered 3D TI Bi_2Se_3 and Bi_2Te_3 ^{14–19} are also good TE materials because of their similar characteristics, such as heavy elements and a small band gap. The helical surface state of 3D TIs has been confirmed using surface sensitive techniques, such as angle-resolved photoemission spectroscopy,^{14–16} scanning tunneling microscopy,^{17–19} and magnetotransport studies.^{20–28} The Dirac surface state is protected by time-reversal symmetry, which enables charge carriers to propagate on the surface or along the edge of a TI without backscattering. Because of the high carrier concentration (10^{19} cm⁻³) of bulk materials, probing the surface conducting channel is a challenging task. Thus, achieving a high-insulating bulk state is a crucial prerequisite for the transport applications of TI and TE materials.

Recently, the BSTS system was confirmed to be a high-insulating bulk TI with high bulk resistivity^{21–23} because of the ordered occupation of Te/Se in the quintuple-layer unit, which substantially cancels the bulk carriers.^{21,23} In addition, the low-dimensional nanostructure with a high surface-to-volume ratio enables metallic surface conduction and TE transport properties to be efficiently probed. In this study, we selected BSTS NWs as our target specimens and expect to observe the novel transport and TE properties therein.

2 Experimental Method

2.1 Nanowire Growth

NWs and nanoribbons were synthesized using a stress-induced method^{29–31}, a catalyst-free growth mechanism based on the mismatch of thermal expansion coefficients between a target film and substrate during a thermal annealing process. The

thermally induced stress stimulated mass flow along the grain boundaries to form NWs or nanoribbons. The BSTS thin film was deposited using the pulsed laser deposition (PLD) method with 140 mJ at a frequency of 10 Hz. The BSTS bulk for the PLD target was grown using the Bridgman method with mixed Bi, Sb, Te, and Se powder 5N (99.999%) at a molar ratio of 1.5:0.5:1.7:1.3 in sealed evacuated quartz tubes. The sample was heated to 800 °C for 48 h, followed by cooling slowly to 500 °C and then annealed at that temperature for 96 h.

Fig. 1a shows a scanning electron microscope (SEM) image of the as-grown NWs several tens of micrometers in length and with diameters ranging from 50 to 300 nm. Straight and uniform BSTS NWs with a high aspect ratio were formed. The high-resolution transmission electron microscopy (TEM) image and the selected area electron diffraction (SAED) pattern revealed that the BSTS NWs were high-quality single-crystalline in a rhombohedral structure with the space group D_{3d}^5 ($R\bar{3}m$) grown along the [110] direction (Fig. 1b). The electron dispersion spectroscopy (EDS) line scan profile (Fig. 1c) and elemental mapping images of the BSTS NW (Fig. 1d) indicated that the Bi, Sb, Te, and Se were uniformly distributed throughout the NW. Furthermore, the EDS point scanning of the NWs revealed that the atomic ratio of Bi/Sb/Te/Se was 1.5 (± 0.3):0.36(± 0.2):1.63(± 0.3):1.01(± 0.02), which is approximately close to the nominal values of 1.5, 0.5, 1.7, and 1.3, respectively. Fig. 2a shows an SEM image of the device for the Seebeck coefficient and resistivity measurements of a single NW. A line heater was placed on the right hand side of the NW to create temperature difference across it; the temperatures at two ends of the NW were monitored using two thermometers by the side. The resistance was measured by the four probe method. Fig. 2b shows a high-magnification SEM image of thermometer 1.

2.2 Device fabrication

The NW specimens were mechanically transferred to the SiO₂ (300 nm)/Si substrate with predefined marks. The electrical contacts were defined using electron-beam lithography and thermal evaporation of Ti/Au.

2.3 Thermoelectric measurements

Magnetotransport measurements were conducted using a quantum design physical property measurement system. The Seebeck coefficient of bulk material and NWs were measured using a conventional steady-state method in an Oxford cryostat. The bulk TE properties were also measured using commercial equipment ZEM-3 (ULVAC-RIKO, Japan). The thermal conductivity κ of BSTS bulk material was calculated using the formula $\kappa = D \times C_p \times d$, where D is the thermal diffusivity, C_p is the specific heat, and d is the density of the sample. The term D was measured using a laser flash apparatus (NETZSCH, LFA 457). The NW thermal conductivity was measured using the 3ω method.^{32,33} (See the ESI† for details of the 3ω method.)

3 Results and Discussion

3.1 Temperature dependence of resistance

According to the SEM image of the NW, the cross-section is approximately circular for NW1 with diameter $d=180$ nm (Fig. 2c) and ribbon-like for NW2 with width $w=110$ nm thickness $t=375$ nm (See the ESI†), which is approximately equivalent to a diameter $d=230$ nm nanowire having the same cross section area. The temperature dependence of resistivity for the BSTS NWs is shown in Fig. 3a. The transport behavior of NW1 and NW2 revealed

semiconductor-like behavior at less than 300 K, indicating insulating behavior, but it saturated and further decreased as the

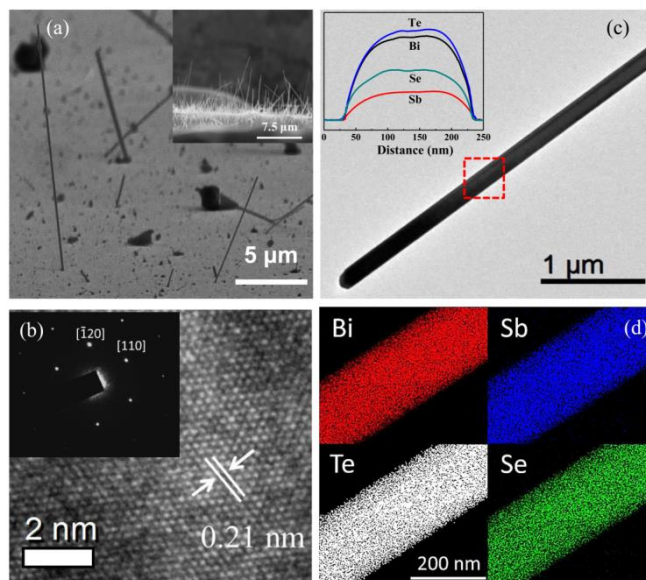


Fig. 1 (a) A SEM image of the as-grown NWs. The inset shows a side view of the as-grown NWs. (b) High-resolution TEM image of the BSTS NW showing a clear crystalline structure. The SAED pattern (top left) shows the sharp diffraction spots, indicating that the high-quality single-crystal BSTS NW grew in the [110] direction. (c) The scanning TEM images of a BSTS NW. The line profiles show that the Bi, Sb, Se, and Te are homogeneously distributed throughout the NW. (d) The elemental mapping obtained from the EDS scan reveals that Bi, Sb, Se, and Te are uniformly distributed in the BSTS NW.

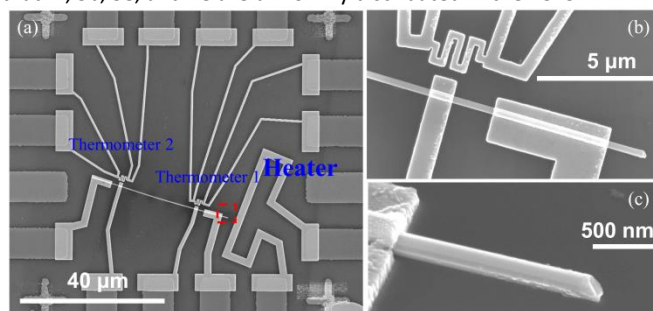


Fig. 2 (a) A SEM image of the device for Seebeck coefficient and electrical conductivity measurements. (b) High magnification SEM image of thermometer 1. (c) Cross-section SEM image of the dashed line area of Fig. 2(a).

temperature decreased to less than 50 K, revealing an additional conduction channel (inset of Fig. 3a).²⁷ From the fitting of resistance to a 3D variable-range hopping model (3D VRH) with R is approximately $\sim e^{(T/T_0)^{-1/4}}$, and a significant deviation occurred at less than 150 K and 120 K for NW1 and NW2, respectively, indicating the existence of a parallel metallic conduction of surface states (inset in Fig. 3b).²³ In addition, the total sheet conductance G_{\square} of TI with thickness t can be formulated as $G_{\square} = G_s + \sigma_b t$, where G_s is the surface sheet conductance and σ_b is the bulk conductivity. For quantitative calculation the equivalent thickness $t \sim 180$ nm for NW1 and $t = 375$ nm for NW2 were used.

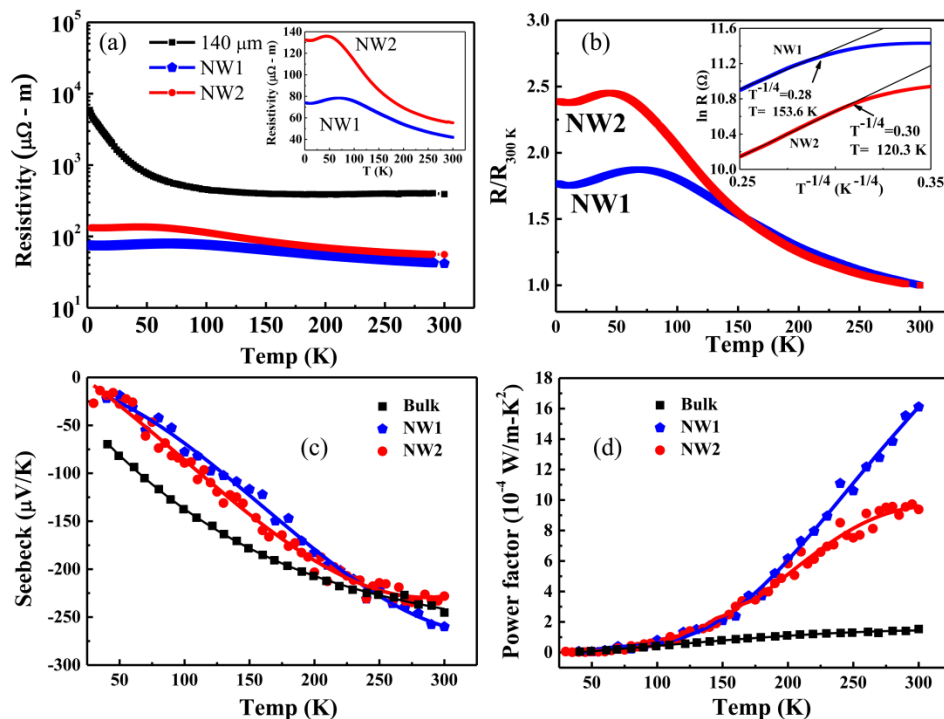


Fig. 3 (a) The temperature dependence of logarithmic resistivity for BSTS specimens of NW1 (180 nm in diameter), NW2 (230 nm in diameter), and the bulk material (thickness of 140 μm). The inset is the resistivity in the linear scale plot for NW1 and NW2. (b) Temperature dependence of the normalized resistance. The inset shows the fitting of the 3D variable-range hopping model. (c) Temperature dependence of the Seebeck coefficient. (d) Temperature dependence of TE PF.

At 2 K, $G_s = 2.5 \times 10^{-4} \Omega^{-1}$, $\sigma_b = 7.52 \Omega^{-1} cm^{-1}$, the surface dominated transport (approximately 94%) approach in BSTS NW1, in which the resistivity decreased by a factor of 80 compared with its bulk. At 300 K, the G_s and σ_b of NW1 and bulk specimen were $G_s = 24.9 \times 10^{-4} \Omega^{-1}$, $\sigma_b = 114.03 \Omega^{-1} cm^{-1}$ and $G_s = 10.95 \times 10^{-4} \Omega^{-1}$, $\sigma_b = 25.49 \Omega^{-1} cm^{-1}$, respectively. The resistivity of NW1 was 10 times lower than its bulk (Fig. 3a)^{22–24} because of nearly 50% surface contribution and the bulk conduction contributed from thermally excited carriers. Remarkably, the stress-induced NW growth method improved the TI surface property and the crystal quality (less disorder); thus, the thermally activated charge carriers provided bulk conduction at room temperature.

3.2 Thermoelectric properties

Heavy elements produce strong spin orbital coupling in TI and produce a low phonon thermal conductivity in TE material. In addition, a small band gap in TE material typically produces a large TE PF, providing an opportunity to modify the band structure of TI; thus, an intrinsic TI material might be a satisfactory TE material and vice versa. The magnitude and temperature dependence of the Seebeck coefficient of NWs was similar to the BSTS bulk material, which monotonically increased as the temperature increased from 40 to 300 K and achieved the bulk value at room temperature (Fig. 3c). The Seebeck coefficient of TI can be formulated using the Boltzmann transport equation⁶:

$$\sigma = e^2 \int_{-\infty}^{\infty} d\varepsilon \left(\frac{\partial f(\varepsilon)}{\partial \varepsilon} \right) \sum(\varepsilon)$$

$$T\sigma S = e \int_{-\infty}^{\infty} d\varepsilon \left(\frac{\partial f(\varepsilon)}{\partial \varepsilon} \right) \sum(\varepsilon)(\varepsilon - E_f)$$

where σ is electrical conductivity and S is the Seebeck coefficient. The term $\sum(\varepsilon) = N(\varepsilon)\tau(\varepsilon)v_x(\varepsilon)^2$ is the conductivity density, and $f(\varepsilon)$ is the Fermi-Dirac distribution function. The ambipolar field effect in TI was comprehensively studied; it yields a sign change in the Hall coefficient and a resistance maximum as the Fermi level crosses the charge neutral point of the symmetry protected surface state. In addition to the Hall coefficient, the Seebeck coefficient changing sign as the Fermi level crosses the Dirac point has recently been demonstrated in a Bi_2Se_3 nanoflake.¹¹ In addition, the theoretical flat-band model¹³ indicated that the Seebeck coefficient achieved a maximal value around the band edges. The high Seebeck coefficient observed in this study indicated that the Fermi levels of the two NWs were near the conduction band minimum, which is consistent with the Shubnikov–de Haas (SdH) oscillation analysis, which is discussed later. Consequently, a TE PF enhanced by a factor of 10 in quasi-1D geometry at room temperature was obtained (Fig. 3d). Table 1 shows the comparison of TE parameters for NWs and BSTS bulk material.

Table 1 Summary of TE parameters for BSTS NWs and bulk material, measured at 300 K.

BSTS	Diameter (nm)	S ($\mu\text{V/K}$)	ρ ($\mu\Omega\text{-m}$)	PF (10^{-4} W/m-K^2)	κ (W/m-K)	ZT
NW 1	180	-259	41.9	16.11	1.33*	0.36
NW 2	230	-228	55.4	9.38	1.33*	0.21
Bulk		-235.8	399.5	1.33	1.4	0.028

*The value is the average of $\kappa = 1.4$ and 1.25 W/m-K for NW4, NW5, respectively (see the ESI†).

3.3 Magnetotransport properties

To understand the nature of surface properties comprehensively, we performed magnetotransport measurements on the NW1 and NW2 specimens. As shown in Fig. 4a, a weak anti-localization (WAL) effect was obtained in the lower field region; the sharp cusps of magnetoresistance (MR) at low temperatures is a signature of the nontrivial Dirac surface state. The WAL in TI is a quantum correction of classical conductance. The spin-momentum locking mechanism in TI resulted from strong spin orbital coupling in which the surface charge carriers acquired a π Berry phase and propagated along the edge or on the surface without backscattering because of the destructive interference of time reversed paths.

The high surface-to-volume ratio in the low-dimensional NWs, in which the bulk carriers were suppressed and produced pronounced SdH oscillations, were revealed in the MR. Fig. 4b shows the temperature dependence of resistance of NW1 after a smooth background subtraction. The SdH oscillations of NW1 and NW2 show a period of $(\Delta 1/B) = 0.0117 \text{ T}^{-1}$ and $(\Delta 1/B) = 0.02683 \text{ T}^{-1}$, respectively, yielding corresponding Fermi surface cross-section areas of $A_F = 8.1 \times 10^{17} \text{ m}^{-2}$ and $A_F = 3.55 \times 10^{17} \text{ m}^{-2}$ according to the Onsager relation. This corresponds to the Fermi wave number $k_F = 0.0507 \text{ \AA}^{-1}$ and 0.0336 \AA^{-1} and a surface carrier density n_{2D} of $2.05 \times 10^{12} \text{ cm}^{-2}$ and $0.89 \times 10^{12} \text{ cm}^{-2}$ for NW1 and NW2, respectively. Fig. 4c shows the Landau level fan diagram plot of $1/B$ versus n for the two NWs. The π Berry phase of the nontrivial topological surface yields the physical origin of SdH oscillations within the intercept of 0.5 in the n axis. The linear fit of the data yields the intercepts of $n = 0.42 \pm 0.12$ for NW1 and 0.43 ± 0.12 for NW2, which are near the ideal Dirac fermions of 0.5. Applying Lifshitz-Kosevich (LK) theory to the SdH amplitudes for NW1 and NW2 with mass $m_c = 0.075 m_0$.²¹ The Dingle analysis revealed the scattering time of $\tau = 6.9 \times 10^{-14} \text{ s}$, which yielded the surface mobility $\mu_s = 1616.4 \text{ cm}^2 \text{ V}^{-1} \text{ s}^{-1}$ and the mean free path $\ell = 54 \text{ nm}$ for NW1. For NW2, $\tau = 8 \times 10^{-14} \text{ s}$, $\mu_s = 1875 \text{ cm}^2 \text{ V}^{-1} \text{ s}^{-1}$, and $\ell = 41 \text{ nm}$. The mean free path obtained in this study is similar to that reported in a previous study.²² Together with m_c and the obtained value k_F of NWs, a Fermi level of 262 meV and 115 meV higher than the Dirac point (Fig. 4d) and the Fermi velocity $v_F = 7.84 \times 10^5 \text{ m/s}$ and $v_F = 5.19 \times 10^5 \text{ m/s}$ for NW1 and NW2, respectively, were obtained. Thus, the high Fermi level positions of NWs are consistent with the results of the high Seebeck coefficient discussed previously.

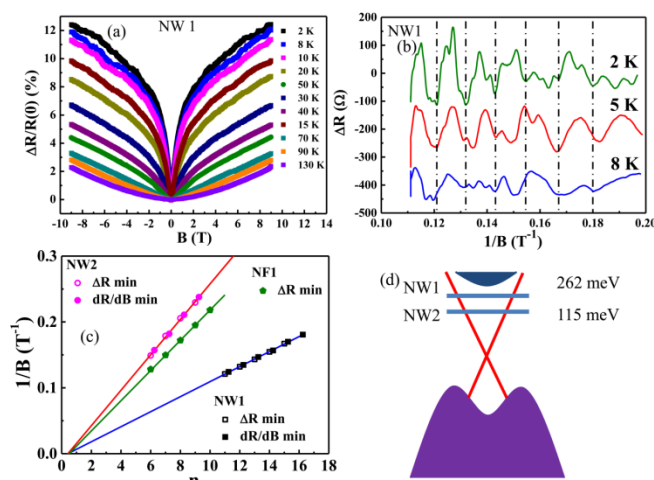


Fig. 4 (a) Transverse magnetoresistance of NW1 for various temperatures. (b) ΔR is a function of $1/B$. (c) The Landau level fan diagram plot. NF1 represents the BSTS nanoflake.²¹ (d) The schematic of the Fermi level positions for NW1 and NW2.

For TIs, the linear part of MR (LMR) usually observed in high magnetic field has been claimed as a result of the surface state.^{28,34–37} Fig. 4a indicates that the MR becomes more linear as the temperature decreases, which can be described using a quadratic equation $MR = a|H| + b/2 H^2$ (in the temperature range of 50 to 130 K). Recently, LMR was determined to be controlled by mobility and was independent of carrier density, which is complementary to the Hall effect.³⁸ The LMR can help determine the mobility and carrier density of NWs.²⁸ As shown in Fig. 5a, we plotted the conventional mobility (μ_{MR}) by the extraction of MR mobility^{39,40} and the linear mobility (μ_{LMR}) fitted from the slope dMR/dH as a function of temperature. The two sets of data coincided perfectly with each other, indicating identical power law dependence. The increase in the mobility of the two NWs as the temperature decreased indicated that phonon scattering dominated in the high temperature region instead of defect scattering. We further plotted the carrier density, as shown in Fig. 5b, according to the obtained value of mobility. Both the trend and magnitude observed in the temperature dependence of carrier density and mobility agreed favorably with those of its nanoflake (see the ESI†). The lower carrier concentration further supported the high PF obtained in this study.

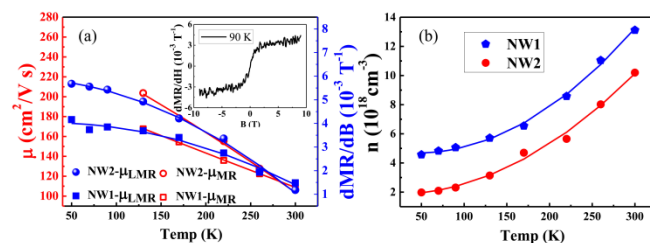


Fig. 5 (a) Extraction of MR mobility and linear part (LMR) of MR of the NWs. (b) The temperature dependence of carrier concentration.

The TE transport properties of TIs are the combination of surface and bulk components. We quantitatively analyzed the data of NWs from a bulk viewpoint. The mobility of the NWs was similar to that of the bulk material ($100 \text{ cm}^2 \text{ V}^{-1} \text{ s}$) at 300 K; however, the carrier density of the NWs ($14 \times 10^{18} \text{ cm}^{-3}$) was 10 times higher without degrading Seebeck coefficient and mobility, which should be degraded by increasing carrier density by using the Mott relation,⁷

$$S = \frac{\pi^2 k_B}{3 q} k_B T \left(\frac{d[\ln(\sigma(E))]}{dE} \right)_{E=E_F} = \frac{\pi^2 k_B}{3 q} k_B T \left(\frac{1}{n} \frac{dn(E)}{dE} + \frac{1}{\mu} \frac{d\mu(E)}{dE} \right)_{E=E_F}$$

This result is attributed to the high density of state and its derivative as the Fermi level near the bulk conduction band edge.

4 Conclusions

In summary, we synthesized high-quality single-crystalline TI BSTS NWs by using a stress-induced method. There is no need to have thin films to open the gap as proposed.⁶ The presence of topological surface state was clearly indicated by magnetotransport measurements. The enhanced thermoelectric figure of merit was observed in the high crystal quality NWs, due to the surface dominated transport and high insulating bulk state in the nanowires. From the MR analysis, the high mobility and low carrier density obtained in the two NWs produced a consistently large TE PF. At room temperature, the two NWs exhibited an intrinsic bulk Seebeck coefficient; specifically, the gapless surface state and high Fermi level positions near the bottom of the conduction band were its physical origins.

Additional studies investigating the thermal conductivity with distinct cross-sectional areas are required. The thermal conductivity has been shown to be substantially reduced in NWs.^{8,9} Thus, together with the reduction of κ in NW and PF enhancement observed in this study, the novel properties of TI provide a promising direction to enhance TE ZT further. The high-insulating bulk state in the BSTS provides a foundation for TE property studies and facilitates the development of low-power-consumption spintronic devices and quantum computation applications.

Acknowledgments

We thank Rajeshkumar Mohanraman, Hung-Shen Chang, and Li Zhao for their valuable contributions. This work was supported by the National Science Council, Taiwan (Grant Number NSC 100-2112 -M-001-019- MY3). Technical support was provided by the instrument center and the Core Facilities for Nanoscience and Nanotechnology at Academia Sinica, Taiwan.

Notes

^a Department of Physics, National Taiwan University, Taipei 106, Taiwan.

^b Nano Science and Technology Program, Taiwan International Graduate Program, Academia Sinica, Taipei, Taiwan and National Taiwan University, Taipei, Taiwan

^c Institute of Physics, Academia Sinica, Taipei 11529, Taiwan.

^d Department of Physics, National Tsing Hua University, Hsinchu 30013, Taiwan

^e Graduate Institute of Applied Physics, National Chengchi University, Taipei 116, Taiwan

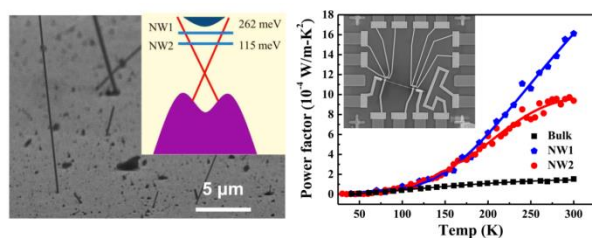
†Electronic Supplementary Information (ESI) available: The supplementary materials contain magnetoresistance and thermal conductivity measurements of additional samples. See DOI: 10.1039/b000000x/

References

- J. E. Moore, *Nature (London)*, 2010, **464**, 194.
- M. Z. Hasan and C. L. Kane, *Rev. Mod. Phys.*, 2010, **82**, 3045.
- X. L. Qi and S. C. Zhang, *Phys. Today*, 2010, **63**, No. 1, 33.
- L. Fu and C. L. Kane, *Phys. Rev. Lett.*, 2008, **100**, 096407.
- T. D. Stanescu, J. D. Sau, R. M. Lutchyn and S. D. Sarma, *Phys. Rev. B: Condens. Matter Mater. Phys.*, 2010, **81**, 241310(R).
- P. Ghaemi, R. S. K. Mong and J. E. Moore, *Phys. Rev. Lett.*, 2010, **105**, 166603.
- J. P. Heremans, V. Jovovic, E. S. Toberer, A. Saramat, K. Kurosaki, A. Charoenphakdee, S. Yamanaka and G. J. Snyder, *Science*, 2008, **321**, 554.
- A. I. Hochbaum, R. K. Chen, R. D. Delgado, W. J. Liang, E. C. Garnett, M. Najarian, A. Majumdar and P. D. Yang, *Nature (London)*, **451**, 163 (2008).
- J. W. Roh, S. Y. Jang, J. Kang, S. Lee, J. S. Noh, W. Kim, J. Park and W. Lee, *Appl. Phys. Lett.*, 2010, **96**, 103101.
- L. D. Hicks and M. S. Dresselhaus, *Phys. Rev. B: Condens. Matter Mater. Phys.*, 1993, **47**, 16631.
- D. Kim, P. Syers, N. P. Butch, J. Paglione and M. S. Fuhrer, *Nano Lett.*, 2014, **14**, 1701.
- B. Hamdoui, J. Kimling, A. Dorn, E. Pippel, R. Rostek, P. Woias and K. Nielsch, *Adv. Mater.*, 2013, **25**, 239.
- M. T. Pettes, J. Maassen, I. Jo, M. S. Lundstrom and L. Shi, *Nano Lett.*, 2013, **13**, 5316.
- Y. Xia, D. Qian, D. Hsieh, L. Wray, A. Pal, H. Lin, A. Bansil, D. Grauer, Y. S. Hor, R. J. Cava and M. Z. Hasan, *Nature Phys.*, 2009, **5**, 398.
- Y. L. Chen, J. G. Analytis, J.-H. Chu, Z. K. Liu, S.-K. Mo, X. L. Qi, H. J. Zhang, D. H. Lu, X. Dai, Z. Fang, S. C. Zhang, I. R. Fisher, Z. Hussain and Z.-X. Shen, *Science*, 2009, **325**, 178.
- D. Hsieh, Y. Xia, D. Qian, L. Wray, F. Meier, J. H. Dil, J. Osterwalder, L. Patthey, A. V. Fedorov, H. Lin, A. Bansil, D. Grauer, Y. S. Hor, R. J. Cava and M. Z. Hasan, *Phys. Rev. Lett.*, 2009, **103**, 146401.
- Z. Alpichshev, J. G. Analytis, J. H. Chu, I. R. Fisher, Y. L. Chen, Z. X. Shen, A. Fang and A. Kapitulnik, *Phys. Rev. Lett.*, 2010, **104**, 016401.
- T. Zhang, P. Cheng, X. Chen, J.-F. Jia, X. Ma, K. He, L. Wang, H. Zhang, X. Dai, Z. Fang, X. Xie and Q.-K. Xue, *Phys. Rev. Lett.*, 2009, **103**, 266803.
- Y. Zhang, K. He, C. Z. Chang, C. L. Song, L. L. Wang, X. Chen, J. F. Jia, Z. Fang, X. Dai, W. Y. Shan, S. Q. Shen, Q. Niu, X. L. Qi, S. C. Zhang, X. C. Ma and Q. K. Xue, *Nature Phys.*, 2010, **6**, 584.
- A. A. Taskin, S. Sasaki, K. Segawa and Y. Ando, *Phys. Rev. Lett.*, 2012, **109**, 066803.
- T. C. Hsiung, D. Y. Chen, L. Zhao, Y. H. Lin, C. Y. Mou, T. K. Lee, M. K. Wu and Y. Y. Chen, *Appl. Phys. Lett.*, 2013, **103**, 163111.
- A. A. Taskin, Z. Ren, S. Sasaki, K. Segawa and Y. Ando, *Phys. Rev. Lett.*, 2011, **107**, 016801.
- Z. Ren, A. A. Taskin, S. Sasaki, K. Segawa and Y. Ando, *Phys. Rev. B: Condens. Matter Mater. Phys.*, 2011, **84**, 165311.
- B. Xia, P. Ren, A. Sulaev, P. Liu, S.-Q. Shen and L. Wang, *Phys. Rev. B: Condens. Matter Mater. Phys.*, 2013, **87**, 085442.
- C. H. Lee, R. He, Z. H. Wang, R. L. J. Qiu, A. Kumar, C. Delaney, B. Beck, T. E. Kidd, C. C. Chancey, R. M. Sankaran and X. P. A. Gao, *Nanoscale*, 2013, **5**, 4337.
- S.-K. Jerng, K. Joo, Y. Kim, S.-M. Yoon, J. H. Lee, M. Kim, J. S. Kim, E. Yoon, S.-H. Chun and Y. S. Kim, *Nanoscale*, 2013, **5**, 10618.
- Z. Wang, R. L. J. Qiu, C. H. Lee, Z. Zhang and X. P. A. Gao, *ACS Nano*, 2013, **7**, 2126.
- H. Tang, D. Liang, R. L. J. Qiu and X. P. A. Gao, *ACS Nano*, 2011, **5**, 7510.
- W. Shim, J. Ham, K. Lee, W. Jeung, M. Johnson and W. Lee, *Nano Lett.*, 2009, **9**, 18.
- J. Ham, W. Shim, D. H. Kim, S. Lee, J. Roh, S. W. Sohn, K. H. Oh, P. W. Voorhees and W. Lee, *Nano Lett.*, 2009, **9**, 2867.
- Dedi, P. C. Lee, C. H. Chien, G. P. Dong, W. C. Huang, C. L. Chen, C. M. Tseng, S. R. Harutyunyan, C. H. Lee and Y. Y. Chen, *Appl. Phys. Lett.*, 2013, **103**, 023115.
- L. Lu, W. Yi, D. L. Zhang, *Rev. Sci. Instrum.*, 2001, **72**, 2996.
- G. Li, D. Liang, R. L. J. Qiu and X. P. A. Gao, *Appl. Phys. Lett.*, 2013, **102**, 043104.
- X. Wang, Y. Du, S. Dou and C. Zhang, *Phys. Rev. Lett.*, 2012, **108**, 266806.
- D.-X. Qu, Y. S. Hor, J. Xiong, R. J. Cava and N. P. Ong, *Science*, 2010,

- 329, 821.
- 36 C. Shekhar, S. Ouardi, A. K. Nayak, G. H. Fecher, W. Schnelle and C. Felser, *Phys. Rev. B: Condens. Matter Mater. Phys.*, 2012, **86**, 155314.
- 37 C. Shekhar, S. Ouardi, G. H. Fecher, A. K. Nayak, C. Felser and E. Ikenaga, *Appl. Phys. Lett.*, 2012, **100**, 252109.
- 38 H. G. Johnson, S. P. Bennett, R. Barua, L. H. Lewis and D. Heiman, *Phys. Rev. B: Condens. Matter Mater. Phys.*, 2010, **82**, 085202.
- 39 L. Thevenod, M. Cassé, W. Desrat, M. Mouis, G. Reibold, D. K. Maude and F. Boulanger, *Appl. Phys. Lett.*, 2007, **90**, 152111.
- 40 Y. M. Meziani, J. Lusakowski, W. Knap, N. Dyakonova, F. Teppe, K. Romanjek, M. Ferrier, R. Clerc, G. Ghibaudo, F. Boeuf and T. Skotnicki, *J. Appl. Phys.*, 2004, **96**, 5761.

Table of contents entry



Thermoelectric transport measurements of topological insulator $\text{Bi}_{1.5}\text{Sb}_{0.5}\text{Te}_{1.7}\text{Se}_{1.3}$ nanowires reveal an enhancement of the thermoelectric figure of merit as compared with its bulk specimen.